THE JOURNAL OF PHYSICAL CHEMISTRY C
A JOURNAL OF THE AMERICAN CHEMICAL SOCIETY

pubs.acs.org/JPCC

Article

Plasmonic Heating Effects in Tip-Enhanced Raman Spectroscopy (TERS)

Published as part of The Journal of Physical Chemistry virtual special issue "Nanophotonics for Chemical Imaging and Spectroscopy".

Joel Rigor, Dmitry Kurouski,* and Nicolas Large*

Cite This: *J. Phys. Chem. C* 2022, 126, 13986–13993

Read Online

ACCESS | Metrics & More | Article Recommendations | Supporting Information

ABSTRACT: Tip-enhanced Raman spectroscopy (TERS) is a spectroscopy technique that possesses single-molecule sensitivity and subnanometer spatial resolution. These unique properties are achieved thanks to the extremely high electromagnetic field confinement at the apex of the scanning probe. However, such strong field confinement can lead to photodecomposition and thermal decomposition of the analytes. Here, we demonstrate that the use of an aqueous solvent as tip−sample junction mediator drastically reduces possible molecule degradation. Using a combination of electrodynamic and heat transport simulations, we provide some theoretical insight into the plasmonic heating of the TERS system. The simulations of a realistic model system show that upon illumination of the tip−sample junction the temperature at the tip apex can increase by ∼180 K when TERS is performed in air with optical powers of ∼100 μW. On the other hand, in aqueous media, the temperature increase of the tip remains significantly lower (a few kelvins) thanks to the higher thermal conductivity of water.

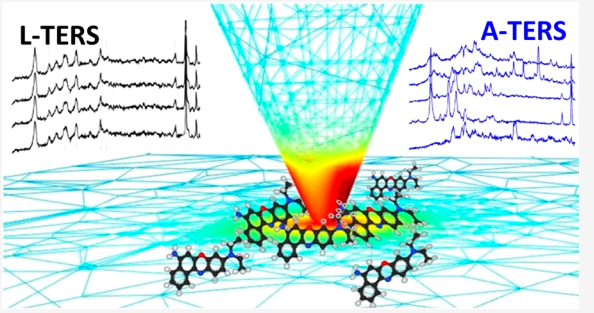

INTRODUCTION

Tip-enhanced Raman spectroscopy (TERS) has being extensively utilized in various research areas ranging from biochemistry and electrochemistry to art conservation and surface science.[1−7] It has been very successful at unraveling new physics and fundamental mechanisms such as structural changes in individual molecules caused by a loss or gain of an electron[8] and hot carrier-driven catalytic reactions on plasmonic and bimetallic nanostructures.[9,10] It has also been shown that TERS is a very powerful, noninvasive technique capable of detecting and identifying dyes directly in artwork,[11] and revealing the structural organization of amyloid and collagen fibrils.[9,10,12−15] However, practical applications of TERS can also be challenging. For example, several research groups reported that vibrational bands in TER spectra can shift by approximately ±7 cm^{-1} relative to their corresponding bands in Normal Raman (NR) spectra.[11,16] Such band shifts often make unambiguous band assignment, especially in the highly complicated TER spectra of biological specimens, extremely challenging. The origin of these band fluctuations is not yet clear, but it has been proposed that such band shifts can be due to molecule−metal interactions and incident light polarization.[16] Another commonly observed issue is photodegradation and thermal degradation of the analyzed specimens.[17−19] This issue was earlier raised in a review article by Pettinger et al.,[4] where the authors noted that the average intensity in the focal area (i.e., tip−substrate junction) reaches values of more than 1.4×10^6 W/cm^2, which corresponds to TERS enhancement factors up to 5×10^9. They also noted that the local field intensity may reach values up to 8×10^{10} W/cm^2 and raised the question of whether molecules could withstand such extreme field strengths. A direct consequence of the strong localization of the electromagnetic fields around a plasmonic system is photothermal heating.[20,21] Photothermal effects are important in almost all plasmonic applications. They can either be beneficial and used for nanoscale thermometry and hyperthermia therapy or be detrimental by causing material deterioration and decreasing the device optical performance. The latter is a significant concern in sensing, imaging, and enhanced spectroscopies.[18−27] Because of the large light absorption increase induced by the localized surface plasmon resonances (LSPRs), a plasmonic system becomes a heat source.[21] This results in a localized temperature increase of tens or hundreds of degrees at the metal surface and in its vicinity, which can have a direct impact on various physical

Received: June 4, 2022
Revised: July 21, 2022
Published: August 4, 2022

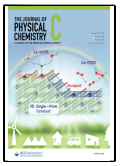

https://doi.org/10.1021/acs.jpcc.2c03881
J. Phys. Chem. C 2022, 126, 13986−13993

processes.[10,28] It can also have drastic effects on the surrounding environment and induce polymer reconfiguration[29] and molecular degradation.[19] In TERS, such degradation can be observed not only in gap mode, where metallic substrates are used to achieve additional enhancement of the TER signal, but also in a nongap-mode (Figure S1, Supporting Information). In the nongap-mode configuration, the use of nonplasmonic substrates such as glass or indium tin oxide (ITO) films allows for a decrease in the intensity of the electromagnetic field at the tip−sample junction.[12,15,30,31] As a result, nongap-mode TERS is often used for structural characterization of heat-sensitive biological samples.[8,12]

In conventional TERS, the tip−sample junction is surrounded by atmospheric air (A-TERS). Since air is a poor heat conductor, one can expect that under such conditions the analyzed specimens can be prone to photodegradation and thermal degradation. Moreover, in A-TERS, the tip−sample junction is open to dust and various air pollutants, which may partially contribute to randomly appearing peaks in the spectra. On the other hand, water possesses a much higher thermal conductivity (κ_{water} = 0.58 W/(m K)) than air (κ_{air} = 0.024 W/(m K)) at 300 K. Therefore, one can expect that the use of aqueous solvents as TERS mediator should facilitate the heat dissipation from the tip−sample junction and, consequently, prevent sample degradation.

Here, we examine this hypothesis by performing TERS measurements on a small dye molecule, Nile Blue (NB), in both air (A-TERS) and aqueous media (L-TERS), as shown in Figure 1A. In our experiments, NB was deposited from ethanolic solutions onto freshly cleaned ITO and glass coverslips.[31] NB is resonant around 633 nm, the excitation wavelength used in this work. Therefore, one can expect that under resonant Raman conditions such molecules could be more sensitive to photodegradation compared to molecular analytes that have no absorption at the excitation wavelength. We performed TERS using an atomic force microscope (AFM-TERS) with Ag and Au probes in air and aqueous solution using the same laser power.

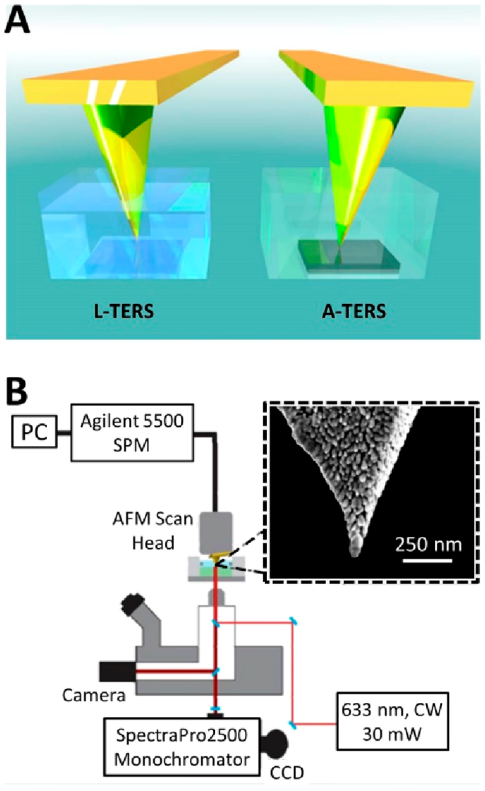

Figure 1. Experimental setup. (A) Diagram of the AFM-TERS apparatus equipped with a 633 nm CW He−Ne laser and TEM image of a typical Au TERS probe. (B) Schematics of TERS measurements in aqueous solution (L-TERS) and air (A-TERS).

METHODS

TERS and SERS. The complete experimental TERS setup is depicted in Figure 1B. Briefly, 633 nm CW light was generated by a He−Ne laser and directed to the microscope objective by a pair of mirrors. The light was then focused on the scanning probe by using 100× oil-immersed Nikon objective installed on a Nikon TE-2000U microscope, which was equipped with a 10/90 beam splitter. Scattered light was collected by using the same objective and was directed through a long-pass filter to the confocal Raman spectrometer (Princeton Instruments, SP2500i) equipped with a 600 grooves/mm grating and a slit entrance set to 100 μm. The dispersed light was then sent to a liquid nitrogen-cooled PI-Acton Spec-10 CCD for spectral acquisition. To obtain a reference SERS spectrum of NB, the molecular analyte was deposited onto a Au film-over-nanoparticles (FON) SERS substrate and dried under room temperature.[6] The SERS spectrum reported in Figure 2 was acquired with the above-described experimental setup using a 633 nm optical excitation at 80 μW.

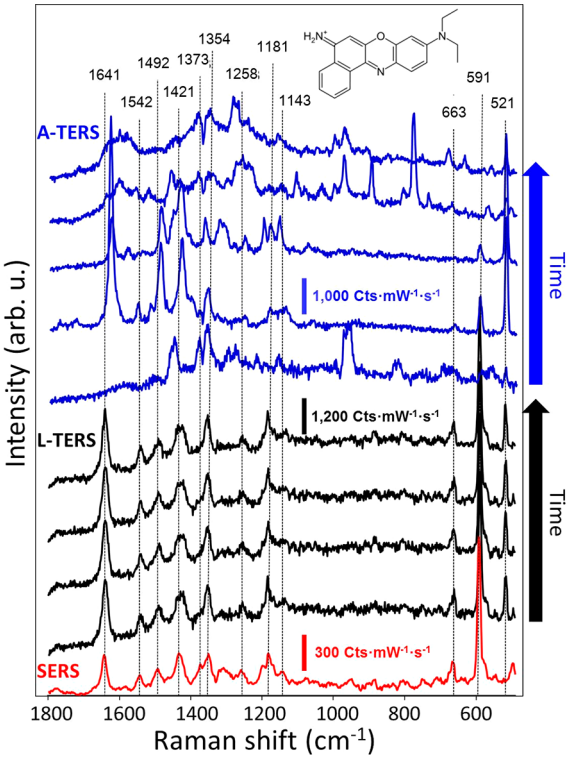

Figure 2. TER spectra of NB on ITO. A-TER (blue) and L-TER (black) spectra of NB acquired in four independently performed experiments; P = 0.11 mW, τ = 1−2 s, λ = 633 nm. Corresponding SER spectrum of NB on AuFON (red); P = 80 μW, τ = 1 s, λ = 633 nm. The arrows indicate the time evolution for the two series of TERS measurements.

https://doi.org/10.1021/acs.jpcc.2c03881
J. Phys. Chem. C 2022, 126, 13986−13993

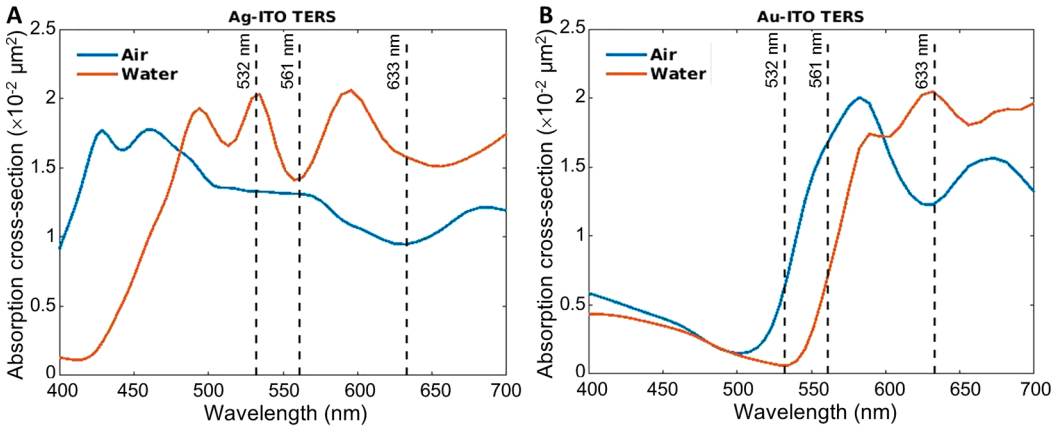

Figure 3. Calculated absorption cross section of the silver (A) and gold (B) TERS tips placed in air (red line) and in water (blue line). The black dashed lines denote the three experimental excitation wavelengths: 532, 561, and 633 nm.

Electrodynamic Simulations. Finite-difference time-domain (FDTD) simulations were performed by using the commercial package by Ansys-Lumerical.[32] The TERS tips were modeled as large and finite conical tips with a tip apex radius of R_{tip} = 25 nm (Figure S2A). The total tip length was set to 1 μm and was extended by a 4 μm cylindrical segment, thus representing a total TERS probe length of 5 μm. At this length, the plasmonic response of the metallic tip converges to the infinite-probe limit as previously shown by Hermann and Gordon.[33] The tip was placed 5 nm above the ITO substrate (taken as semi-infinite). The optical source was taken as a broadband plane wave excitation incident at 30° and linearly polarized in the plane of incidence (p-polarization) as shown in Figure S2A. The FDTD simulation domain was set as a region of 2 × 2 × 6 μm^3 with perfectly matched layers (PMLs) as boundary conditions to mimic an infinite medium. Symmetries were used along the x- and y-directions to minimize the computational cost. A conformal mesh of 1 nm was used in a volume of 200 × 200 × 200 nm^3 around the tip apex to accurately discretize the tip−substrate region and ensure good convergence. An auto-shutoff parameter of 10^{-7} was chosen as convergence parameter, allowing the electromagnetic fields to propagate for about 100 fs. The dielectric permittivities tabulated by Johnson and Christy[34] and by Palik[35] were used for gold and silver, respectively. The ITO substrate was modeled with the dispersive dielectric permittivity reported by König et al.,[36] while air and water were modeled with constant refractive indices of 1.00 and 1.33, respectively.

Heat Transfer Simulations. Finite elements method (FEM) simulations were performed by using the commercial package by Ansys-Lumerical.[32] The gold and silver tips were modeled by using the exact same geometry used in the FDTD calculations (Figure S2A). Au, Ag, and ITO were modeled using thermal conductivities of κ = 406, 315, and 5.9 W/(m K), respectively.[37−39]

A temperature boundary condition was applied at the bottom of the simulation region (bottom of the 100 μm thick substrate) to set it at room temperature (300 K). A constant convective heat transfer coefficient h = 10 W/(m^2 K) was used at the air−metal and air−ITO interfaces, and h = 500 W/(m^2 K) was used at the water−metal and water−ITO interfaces to model the heat loss through convection. Water was modeled with a thermal conductivity of κ_{water} = 0.58 W/(m K).

RESULTS AND DISCUSSION

The A-TER spectra of NB (Figure 2, blue), which were taken at different locations on an ITO substrate, exhibit random peaks that were not evident in the corresponding surface-enhanced Raman (SER) spectrum (Figure 2, red). The intensity of the bands in the acquired A-TER spectra shows significant variations from spectrum to spectrum. At the same time, when TERS is performed in liquid (L-TERS), we did not observe any variation in the intensity of the NB bands, and we did not observe any randomly appearing bands (Figure 2, black). Such additional bands observed in A-TERS are attributed to be the signature of the products resulting from the photodegradation and thermal degradation of NB.

One can expect that in L-TERS NB may diffuse throughout the tip−sample junction since the analyte molecules are not chemically bound to the sample surface. Such diffusion will result in a visible lack of molecule decomposition. However, previous experiments demonstrated that under ambient conditions (A-TERS) a water meniscus is formed at the tip−sample junction.[40] Therefore, molecular diffusion may take place in both A- and L-TERS experiments. In contrast, we demonstrated in a previous study that NB strongly interacts with the ITO surface and does not diffuse from it.[31] This allows us to confidently rule out the possibility of NB diffusion throughout the tip−sample junction in both A- and L-TERS experiments.

The probes used in these TERS measurements (inset, Figure 1B) were fabricated through simple thermal evaporation of 70 nm of Au on the silicon tip in the vacuum chamber. This method results in a continuous metal film on the surface of such scanning probes, It should be also noted that results reported in Figure 2 were reproducible for more than 20 scanning probes (in both A- and L-TERS). These results also suggest that temperature, rather than the LSPR of the scanning probe, was the major contributor to the observed differences between A- and L-TERS experiments.

Stiles et al. investigated the spectral changes in the LSPRs of individual nanoprisms upon their immersion in water.[40] The change in surrounding medium results in a spectral red-shift of the LSPR. However, no significant broadening of the spectra was observed upon immersion of the nanoprisms. This observation suggests that significant reduction of photo-degradation, which was recently observed for L-TERS as

https://doi.org/10.1021/acs.jpcc.2c03881
J. Phys. Chem. C 2022, 126, 13986−13993

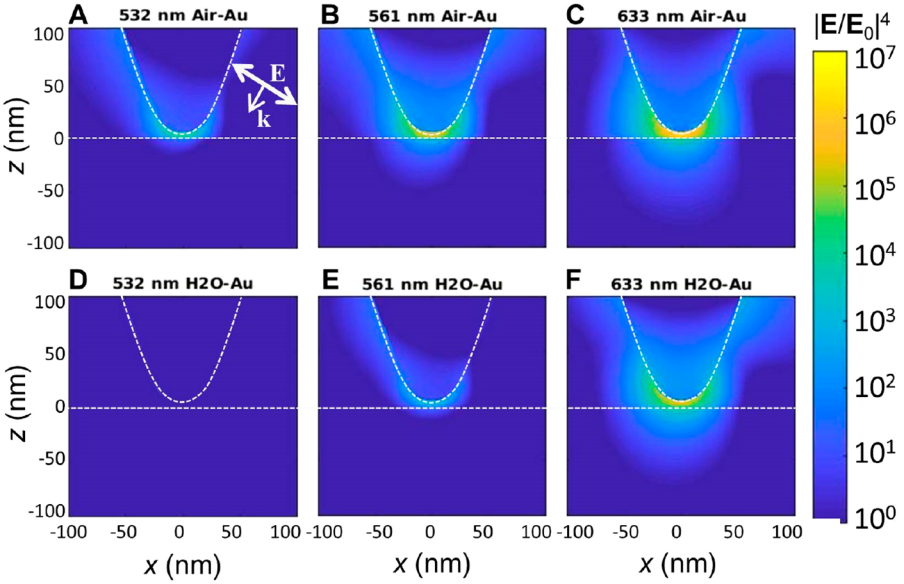

Figure 4. Near-field distributions for a Au tip on a ITO substrate. Calculated near-field ($|\mathbf{E}/\mathbf{E}_0|^4$) spatial distribution around a gold tip in air (A−C) and in water (D−F) for three TERS excitation wavelengths: 532, 561, and 633 nm. The incident optical excitation is polarized linearly as shown in panel A. The profiles of the TERS tip and substrate are highlighted by the white dashed lines.

compared to A-TERS, is not be caused by the damping of the tip LSPR.

We performed electrodynamic simulations using the FDTD method to calculate the optical properties of the TERS tips in the different configurations.

It can easily be noticed from the calculated absorption cross sections (Figure 3) that placing the Ag and Au TERS tips into water instead of air leads to a small spectral shift of the LSPR. This spectral red-shift is well-known and is caused by the change in refractive index of the medium surrounding the plasmonic system (i.e., dielectric screening effect).[41,42] With the spectral shift, we expect that there will be a change in temperature between the systems showing that the surrounding medium has significant effect in the photothermal properties. It is worth noting that because of the angle of incidence, the optical excitation has both a longitudinal and transverse component, thus exciting LSPRs along the longitudinal axis (z-direction; Figure S2B,C) and the transverse axis (x-direction; Figure S2D,E). We also note that some of the laser excitations are off-resonance with the LSPR of each system. From these wavelengths, we expect lower temperatures than those found when exciting the system at their resonance wavelength. However, this does not really alter the near-field intensity and electromagnetic confinement at the vicinity of the metal. Figure 4 shows spatial distribution of the fourth power of the local electric field, $|\mathbf{E}/\mathbf{E}_0|^4$, which gives the TERS enhancement factor, calculated for a Au tip in air (Figure 4A−C) and in water (Figure 4D−F) when excited at three different TERS excitation wavelengths (i.e., 532, 561, and 633 nm). One can note that, as expected, the electric field is localized at the tip apex, close to the substrate and along the tip surface. In our particular modeled system, the FDTD simulations predict a maximum TERS electromagnetic enhancement factor of the order of 10^7, consistent with previous works.[4,7,9]

This plasmonic enhancement makes it possible to detect and perform vibrational studies on extremely small amounts of molecules in TERS. However, one important characteristic of such system is the photothermal heating. The photothermal processes begins with an optical source of excitation incident on the system. Light is then absorbed into the system (thanks to the large absorption cross section of the metal) generating plasmons. In turn, these plasmons induce the intense localized electromagnetic fields found in the tip−substrate junction, which are used for enhancing the Raman signal, and heat through the Joule effect.[20−22,24] While plasmonic heating could be controlled and used in multiple applications,[22,23,43−45] it can be the source of molecular degradation in TERS (Figure 2). One may expect that the intensity ratio of vibrational bands in Stokes versus anti-Stokes TERS spectra can be used to experimentally determine the temperatures at the tip−sample junction. However, recently reported results by Richard-Lacroix and Deckert demonstrated that such measurements are not trivial.[18] Using 16-mercaptohexadodecanoic acid as a molecular reporter, the researchers found that relative intensities of Stokes versus anti-Stokes vibrations depend on the LSPR of the scanning probe. Consequently, without an experimental determination of the LSPR of the TERS tip, such measurements can provide unphysical conclusions (∼2000 K temperature values). It should be noted that the experimental verification of the LSPR of the scanning probe cannot be achieved due to the small optical scattering of the apex nanostructure. Sheldon and co-workers proposed an alternative experimental approach to solve this issue. They demonstrated that spectral background fitting could be used to reveal the plasmon dephasing time and metal lattice temperatures. Nevertheless, there is no clear understanding of the temperature at the tip−samples junction.

In order to estimate the effect of plasmonic heating on the Au and Ag tips, both in air and in water, we used a simple approximation derived for small finite-sized objects.[20,23,24] In this model, we first calculated the heat power (i.e., total absorption rate), Q, from the absorption spectrum (Figure S3):

$$Q = \sigma_{abs} I \tag{1}$$

where I is the laser irradiance and σ_{abs} is the absorption cross section calculated using FDTD. This calculated heat power

https://doi.org/10.1021/acs.jpcc.2c03881
J. Phys. Chem. C 2022, 126, 13986−13993

was then used as heat source to compute the temperature increase resulting from the plasmonic heating as

$$\Delta T(r) = \frac{Q}{4\pi\kappa_0(R_{tip} + r)} \quad (2)$$

where κ_0 is the thermal conductivity of the surrounding medium (i.e., air or water), R_{tip} is the tip radius, and r is the distance from the metallic tip surface.

Although this simple model was developed for finite-size nanoparticles,[24] it is believed to give a qualitative picture and a good approximation of the temperature changes in the vicinity of a rounded tip apex (Figure S3). However, in order to account for all the physical effects involved in the thermal process and properly account for all the thermal decay channels (e.g., conduction via the substrate, conduction via the bulk of the metallic tip, and convection at the medium/metal and medium/substrate interfaces), we performed full thermal simulations using the heat transport module of the Ansys-Lumerical package[32] and following the procedure proposed by Manrique-Bedoya et al.[43] The finite-element method (FEM) solver calculates the temperature, T, solution of Fourier's heat transport equation:

$$\rho(\mathbf{r})c_p(\mathbf{r})\frac{\partial T(\mathbf{r}, t)}{\partial t} - \nabla\cdot[\kappa(\mathbf{r})\nabla T(\mathbf{r}, \mathbf{t})] = q(\mathbf{r}) \quad (3)$$

where ρ is the mass density, c_p is the specific heat, and κ is the thermal conductivity. The function $q(\mathbf{r})$ is the applied heat energy transfer rate (i.e., heat power density) inside the metal and defined as $Q = \int_V q(\mathbf{r})\, d^3r$, where the integral is computed over the volume of the metallic tip, V.

In the system of interest, the steady-state temperature is usually reached very quickly due to its micrometer-scale dimensions. Under continuous wave illumination conditions, the typical duration of the transient regime, τ_{tr}, is not dependent on the temperature increase but rather on the characteristic size of the system. For the micrometer-scale metal tip modeled here, τ_{tr} is of the order of a few microseconds. When performed in steady-state conditions ($\partial T/\partial t = 0$), eq 3 is reduced to a simple Poisson's equation:

$$-\nabla\cdot[\kappa(\mathbf{r})\nabla T(\mathbf{r}, \mathbf{t})] = q(\mathbf{r}) \quad (4)$$

Figure S2 shows the calculated optical power absorbed by the tip−substrate system at the LSPR wavelength (Au: 532 nm in air and 569 nm in water; Ag: 407 nm in air and 471 nm in water) and used as the heat source to describe the applied heat energy transfer rate Q in eq 4. The incident optical power is set to 80 μW, which corresponds to an irradiance I = 13 μW/μm^2. Figure 5 shows the temperature distribution at tip−substrate junction and on the surface of the ITO substrate. This temperature distribution is normalized to its minimum and maximum temperatures for each of the four configurations (i.e., Au/air, Au/water, Ag/air, and Ag/water). The associated color-scale bars are displayed on the right side of the panels. First, it can be noted that the whole metallic tip is thermally uniform and is the hottest part of the system, achieving temperature changes as high as $\Delta T_{Ag/air}$=138 K and $\Delta T_{Au/air}$=69 K for the Ag and Au tips in air, respectively (Figure 5A). When placed in the aqueous solution, the tip temperature is significantly lower than in air; the tip experiences a maximum temperature increase of only a few degrees ($\Delta T_{Au/water}$ = 2.9 K and $\Delta T_{Ag/water}$ = 5.6 K). Second, because of its metallic properties, the ITO substrate also heats

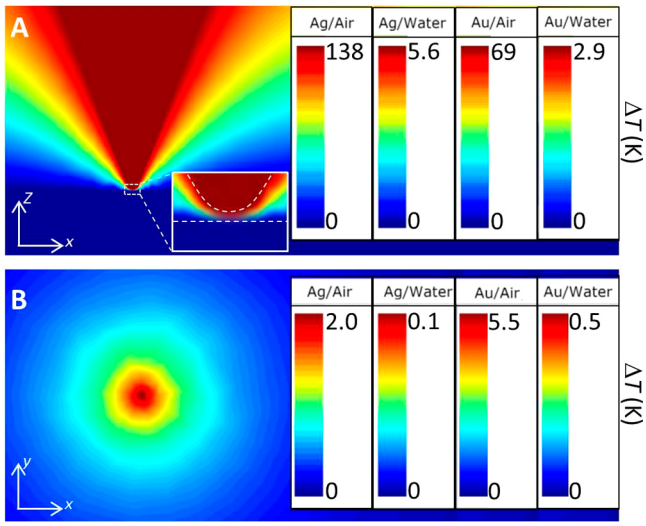

Figure 5. Plasmonic heating effect. Full thermal calculation of the temperature distribution at the tip−substrate junction and at the surface of the metal when optically excited at 633 nm. (A) Vertical cross section in the plane (x,z). Inset: close-up view of the tip−substrate region, showing the temperature gradient in the 5 nm gap. (B) Horizontal cross section in the plane (x,y), taken on the substrate (z = 0). The spatial distribution of temperature change, ΔT, is normalized for each of the four cases (Au/air, Au/water, Ag/air, and Ag/water). The color scales associated with each of these four cases with the corresponding maximum temperature change are shown on the right side.

up slightly, exhibiting a maximum temperature change of the order of $\Delta T_{ITO/air}$ ~ 2−5.5 K, with a hot spot immediately underneath the tip location (Figure 5B). Similarly to the tip, when the substrate is in contact with water, its surface experiences a much lower temperature change. The inset of Figure 5A shows a close-up view of the temperature gradient within the 5 nm gap, which is consistent with the $1/r$ spatial dependence predicted by eq 2. Finally, it is worth noting that the ratio of maximum temperature change on the tip surface in air and water is $\Delta T_{air}/\Delta T_{water}$ = 24, which, unsurprisingly, is the ratio between the thermal conductivities of water and air, $\kappa_{water}/\kappa_{air}$.

With different incident optical powers, we expect there to be an increase in the maximum temperature change throughout the whole system. We performed power dependence calculations in the range 0.01−100 μW to determine the effects of the optical power on the TERS system. Figure 6 shows the effects of increasing the optical power in the TERS systems with Ag (solid lines) and Au (dashed lines) tips in either air (blue) or water (red). We first notice that the temperature increase follows the linear trend from eq 1. Also, there is a significant change between the two systems as the power increases. At 100 μW the A-TERS system reaches a maximum temperature change of ~180 K while the L-TERS system increases by a mere ~8 K. This further shows that the surrounding medium has a significant role on the plasmonic heating effects in the TERS system. It is worth noting that the values of temperature change, obtained from the full heat transfer simulations (Figure 6), are consistent with the temperatures obtained from the simplistic model governed by eq 2 (Figure S3). However, it is important to note that the temperatures calculated here are for idealized systems and that other effects are at play in an experimental configuration. First,

https://doi.org/10.1021/acs.jpcc.2c03881
J. Phys. Chem. C 2022, 126, 13986−13993

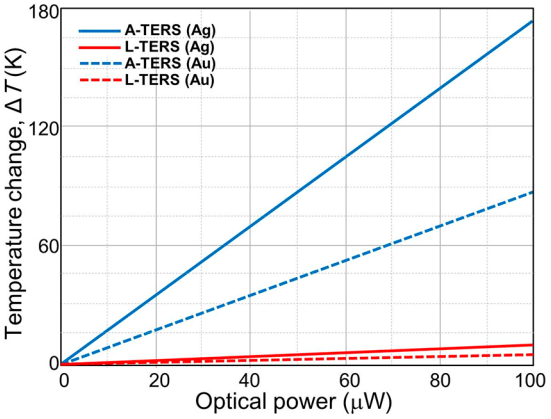

Figure 6. Temperature change at the tip apex as a function of the optical power for L-TERS and A-TERS. Comparisons are made between L-TERS (red) systems and A-TERS (blue) systems for optical powers ranging from 0.01 to 100 μW for both a silver tip (solid lines) and a gold tip (dashed lines). The optical excitation has a wavelength of 633 nm.

while this plasmonic heating model holds for plasmonic nanostructures in homogeneous and infinite media, the medium may not be homogeneous, in particular near the tip−substrate junction. Second, the limits of this model reside in the actual tip−substrate geometry. The actual local morphology of the tip apex as well as its actual composition (e.g., crystallinity, impurities, grain boundaries, etc.) may play role in the heat conduction and dissipation through the metallic tip as well as in the convection efficiency with the surrounding medium.

CONCLUSIONS

In conclusion, we have shown that in A-TERS highly confined electromagnetic fields induced by the LSPR result in very efficient plasmonic heating which led to very high temperatures in the tip−sample junction. Our FDTD simulations show that temperatures, which can reach significant local values of hundreds of kelvins, will likely cause thermal degradation of analytes present in the probe−sample junction. This will lead to the random fluctuations of vibrational bands in the corresponding TERS spectra. On the other hand, when TERS is performed in aqueous solutions (L-TERS), the temperature increase of the tip apex is significantly limited to only a few tens of kelvins, ultimately resulting in a more stable TERS signal over time. Consequently, efficient heat dissipation at the tip−sample junction, via high thermal conductivity media, drastically reduced photodegradation and thermal degradation of analytes in TERS. While these computational models do not account for atomic-scale details (e.g., impurities, crystallinity, and grain boundaries) and remain ideal, as compared to an experimental TERS tip−sample system, they support the use of aqueous solvents as mediators to minimize the photodegradation and thermal degradation of the analytes. They also provide valuable insight as to the extent of the plasmonic heating in enhanced Raman spectroscopies such as TERS and SERS, where local electromagnetic fields are highly localized and enhanced. Photothermal effects, such as plasmonic heating at the nanoscale, represent an interesting problem that affects not only TERS and SERS measurements but also a large number of plasmonic applications in optoelectronics, photonic circuitry, and biomedical applications such as sensing, imaging, and drug delivery. The most challenging remaining problems are associated with (i) the direct experimental measurement of the local temperatures at the metallic surface of the nanostructures and (ii) the fundamental understanding of heat transfer processes through molecules and molecular linkers present at the metallic surface and in its vicinity.

ASSOCIATED CONTENT

Supporting Information

The Supporting Information is available free of charge at https://pubs.acs.org/doi/10.1021/acs.jpcc.2c03881.

(S1) Nongap-mode TER spectra of alizarin: nongap-mode TERS; (S2) electrodynamic simulations: simulation model, absorption cross sections, spectral dependence of heat power and temperature increase, near-field distributions for a Ag tip on a ITA substrate (PDF)

AUTHOR INFORMATION

Corresponding Authors

Dmitry Kurouski − *Department of Biochemistry and Biophysics, Texas A&M University, College Station, Texas 77843, United States;* orcid.org/0000-0002-6040-4213; Email: dkurouski@tamu.edu

Nicolas Large − *Department of Physics and Astronomy, The University of Texas at San Antonio, San Antonio, Texas 78023, United States;* orcid.org/0000-0002-2699-5718; Email: Nicolas.Large@utsa.edu

Author

Joel Rigor − *Department of Physics and Astronomy, The University of Texas at San Antonio, San Antonio, Texas 78023, United States*

Complete contact information is available at: https://pubs.acs.org/10.1021/acs.jpcc.2c03881

Author Contributions

D.K. performed the TERS measurements. J.R. and N.L. performed the electrodynamic and thermal modeling and theoretical analysis. All authors have contributed to writing and editing the manuscript and have given approval to the final version.

Notes

The authors declare no competing financial interest.

ACKNOWLEDGMENTS

This work received financial support from the Army Research Office (ARO) under Grant W911NF-18-1-0439 (N.L.) and National Institute of General Medical Sciences under Grant R35GM142869 (D.K.). This work also received computational support from UTSA's HPC cluster Shamu, operated by the Office of Information Technology. The authors also thank Dr. George C. Schatz and late Dr. Richard P. Van Duyne for the valuable and stimulating discussions and early insights into this work.

REFERENCES

(1) Schmid, T.; Opilik, L.; Blum, C.; Zenobi, R. Nanoscale Chemical Imaging Using Tip-Enhanced Raman Spectroscopy: A Critical Review. *Angew. Chem., Int. Ed.* **2013**, *52* (23), 5940−5954.

(2) Deckert-Gaudig, T.; Deckert, V. Tip-enhanced Raman scattering studies of histidine on novel silver substrates. *J. Raman Spectrosc.* **2009**, *40*, 1446−1451.
(3) Huang, T.-X.; Huang, S.-C.; Li, M.-H.; Zeng, Z.-C.; Wang, X.; Ren, B. Tip-enhanced Raman spectroscopy: tip-related issues. *Anal. Bioanal. Chem.* **2015**, *407*, 8177−8195.
(4) Pettinger, B.; Schambach, P.; Villagómez, C. J.; Scott, N. Tip-Enhanced Raman Spectroscopy: Near-Fields Acting on a Few Molecules. *Annu. Rev. Phys. Chem.* **2012**, *63*, 379−399.
(5) Klingsporn, J. M.; Jiang, N.; Pozzi, E. A.; Sonntag, M. D.; Chulhai, D.; Seideman, T.; Jensen, L.; Hersam, M. C.; Duyne, R. P. V. Intramolecular Insight into Adsorbate−Substrate Interactions via Low-Temperature, Ultrahigh-Vacuum Tip-Enhanced Raman Spectroscopy. *J. Am. Chem. Soc.* **2014**, *136* (10), 3881−3887.
(6) Zrimsek, A. B.; Chiang, N.; Mattei, M.; Zaleski, S.; McAnally, M. O.; Chapman, C. T.; Henry, A.-I.; Schatz, G. C.; Van Duyne, R. P. Single-Molecule Chemistry with Surface- and Tip-Enhanced Raman Spectroscopy. *Chem. Rev.* **2017**, *117* (11), 7583−7613.
(7) Kumar, N.; Su, W.; Veselý, M.; Weckhuysen, B. M.; Pollard, A. J.; Wain, A. J. Nanoscale chemical imaging of solid−liquid interfaces using tip-enhanced Raman spectroscopy. *Nanoscale* **2018**, *10* (4), 1815−1824.
(8) Wang, R.; He, Z.; Sokolov, A. V.; Kurouski, D. Gap-Mode Tip-Enhanced Raman Scattering on Au Nanoplates of Varied Thickness. *J. Phys. Chem. Lett.* **2020**, *11* (10), 3815−3820.
(9) Li, Z.; Rigor, J.; Large, N.; El-Khoury, P. Z.; Kurouski, D. Underlying Mechanisms of Hot Carrier-Driven Reactivity on Bimetallic Nanostructures. *J. Phys. Chem. C* **2021**, *125* (4), 2492−2501.
(10) Wang, R.; Li, J.; Rigor, J.; Large, N.; El-Khoury, P. Z.; Rogachev, A. Y.; Kurouski, D. Direct Experimental Evidence of Hot Carrier-Driven Chemical Processes in Tip-Enhanced Raman Spectroscopy (TERS). *J. Phys. Chem. C* **2020**, *124* (3), 2238−2244.
(11) Kurouski, D.; Zaleski, S.; Casadio, F.; Van Duyne, R. P.; Shah, N. C. Tip-Enhanced Raman Spectroscopy (TERS) for in Situ Identification of Indigo and Iron Gall Ink on Paper. *J. Am. Chem. Soc.* **2014**, *136* (24), 8677−8684.
(12) Kurouski, D.; Deckert-Gaudig, T.; Deckert, V.; Lednev, I. K. Structure and composition of insulin fibril surfaces probed by TERS. *J. Am. Chem. Soc.* **2012**, *134* (32), 13323−9.
(13) Gullekson, C.; Lucas, L.; Hewitt, K.; Kreplak, L. Surface-sensitive Raman spectroscopy of collagen I fibrils. *Biophys. J.* **2011**, *100* (7), 1837−45.
(14) Kurouski, D.; Deckert-Gaudig, T.; Deckert, V.; Lednev, I. K. Surface Characterization of Insulin Protofilaments and Fibril Polymorphs Using Tip-Enhanced Raman Spectroscopy (TERS). *Biophys. J.* **2014**, *106* (1), 263−271.
(15) Deckert-Gaudig, T.; Kämmer, E.; Deckert, V. Tracking of nanoscale structural variations on a single amyloid fibril tip-enhanced Raman scattering. *J. Biophotonics* **2012**, *5*, 215−219.
(16) Deckert, V.; Deckert-Gaudig, T.; Diegel, M.; Götz, I.; Langelüddecke, L.; Schneidewind, H.; Sharma, G.; Singh, P.; Singh, P.; Trautmann, S.; et al. Spatial resolution in Raman spectroscopy. *Faraday Discuss.* **2015**, *177* (0), 9−20.
(17) Fang, M.; Ivanisevic, J.; Benton, H. P.; Johnson, C. H.; Patti, G. J.; Hoang, L. T.; Uritboonthai, W.; Kurczy, M. E.; Siuzdak, G. Thermal Degradation of Small Molecules: A Global Metabolomic Investigation. *Anal. Chem.* **2015**, *87* (21), 10935−10941.
(18) Richard-Lacroix, M.; Deckert, V. Direct molecular-level near-field plasmon and temperature assessment in a single plasmonic hotspot. *Light Sci. Appl.* **2020**, *9* (1), 35.
(19) Sarhan, R. M.; Koopman, W.; Schuetz, R.; Schmid, T.; Liebig, F.; Koetz, J.; Bargheer, M. The importance of plasmonic heating for the plasmon-driven photodimerization of 4-nitrothiophenol. *Sci. Rep.* **2019**, *9* (1), 3060.
(20) Govorov, A. O.; Richardson, H. H. Generating heat with metal nanoparticles. *Nano Today* **2007**, *2* (1), 30−38.
(21) Baffou, G.; Quidant, R. Thermo-plasmonics: using metallic nanostructures as nano-sources of heat. *Laser Photon. Rev.* **2013**, *7* (2), 171−187.
(22) García-Rosas, C. M.; Medina, L. A.; Lopez, P.; Large, N.; Reyes-Coronado, A. Magneto-plasmonic biocompatible nanorice. *J. Nanopart. Res.* **2021**, *23* (7), 144.
(23) Baffou, G.; Quidant, R.; García de Abajo, F. J. Nanoscale control of optical heating in complex plasmonic systems. *ACS Nano* **2010**, *4* (2), 709−716.
(24) Baffou, G.; Quidant, R.; Girard, C. Heat generation in plasmonic nanostructures: Influence of morphology. *Appl. Phys. Lett.* **2009**, *94* (15), 153109−153109.
(25) Baffou, G.; Quidant, R.; Girard, C. Thermoplasmonics modeling: A Green's function approach. *Phys. Rev. B* **2010**, *82* (16), 165424.
(26) Abid, I.; Chen, W.; Yuan, J.; Najmaei, S.; Peñafiel, E. C.; Péchou, R.; Large, N.; Lou, J.; Mlayah, A. Surface enhanced resonant Raman scattering in hybrid MoSe2@Au nanostructures. *Opt. Express* **2018**, *26* (22), 29411−29423.
(27) Lopez, P.; Mayer, K.; Large, N. In Synthesis, Characterization, and Computational Modeling of Polyelectrolyte-Coated Plasmonic Gold Nanorods for Photothermal Heating Studies. *Proc. SPIE* **2019**, 168−172.
(28) Abid, I.; Chen, W.; Yuan, J.; Bohloul, A.; Najmaei, S.; Avendano, C.; Péchou, R.; Mlayah, A.; Lou, J. Temperature dependent plasmon-exciton interactions in hybrid Au/MoSe2 nanostructures. *ACS Photonics* **2017**, *4* (7), 1653−1660.
(29) Bustamante, G.; Carrizales, K.; DeLuna, F.; Large, N.; Ye, J. Y. In Fabrication and Characterization of Thermo-Responsive Gold Nanorod Assemblies. *Proc. SPIE* **2018**, 23−32.
(30) Kurouski, D.; Postiglione, T.; Deckert-Gaudig, T.; Deckert, V.; Lednev, I. K. Amide I vibrational mode suppression in surface (SERS) and tip (TERS) enhanced Raman spectra of protein specimens. *Analyst* **2013**, *138* (6), 1665−1673.
(31) Kurouski, D.; Mattei, M.; Van Duyne, R. P. Probing Redox Reactions at the Nanoscale with Electrochemical Tip-Enhanced Raman Spectroscopy. *Nano Lett.* **2015**, *15* (12), 7956−62.
(32) Ansys-Lumerical, Inc. https://www.lumerical.com/.
(33) Hermann, R. J.; Gordon, M. J. Quantitative comparison of plasmon resonances and field enhancements of near-field optical antennae using FDTD simulations. *Opt. Express* **2018**, *26* (21), 27668−27682.
(34) Johnson, P. B.; Christy, R. W. Optical Constants of the Noble Metals. *Phys. Rev. B* **1972**, *6* (12), 4370−4379.
(35) Lynch, D. W.; Hunter, W. R. In *Handbook of Optical Constants of Solids*; Palik, E. D., Ed.; Academic Press: Burlington, MA, 1997; Vol. *1*, pp 275−367.
(36) König, T. A.; Ledin, P. A.; Kerszulis, J.; Mahmoud, M. A.; El-Sayed, M. A.; Reynolds, J. R.; Tsukruk, V. V. Electrically tunable plasmonic behavior of nanocube-polymer nanomaterials induced by a redox-active electrochromic polymer. *ACS Nano* **2014**, *8* (6), 6182−92.
(37) Choi, S. K.; Lee, J. I. Effect of film density on electrical properties of indium tin oxide films deposited by dc magnetron reactive sputtering. *J. Vac. Sci. Technol. A* **2001**, *19*, 2043.
(38) Yagi, T.; Tamano, K.; Sato, Y.; Taketoshi, N.; Baba, T.; Shigesato, Y. Analysis on thermal properties of tin doped indium oxide films by picosecond thermoreflectance measurement. *J. Vac. Sci. Technol. A* **2005**, *23* (4), 1180−1186.
(39) Ashida, T.; Miyamura, A.; Oka, N.; Sato, Y.; Yagi, T.; Taketoshi, N.; Baba, T.; Shigesato, Y. Thermal transport properties of polycrystalline tin-doped indium oxide films. *J. Appl. Phys.* **2009**, *105* (7), 073709.
(40) Stiles, R. L.; Willets, K. A.; Sherry, L. J.; Roden, J. M.; Van Duyne, R. P. Investigating Tip-Nanoparticle Interactions in Spatially Correlated Total Internal Reflection Plasmon Spectroscopy and Atomic Force Microscopy. *J. Phys. Chem. C* **2008**, *112*, 11696−11701.
(41) Martinsson, E.; Shahjamali, M. M.; Large, N.; Zaraee, N.; Zhou, Y.; Schatz, G. C.; Mirkin, C. A.; Aili, D. Influence of Surfactant

Bilayers on the Refractive Index Sensitivity and Catalytic Properties of Anisotropic Gold Nanoparticles. *Small* **2016**, *12* (3), 330−342.
(42) Miller, M. M.; Lazarides, A. A. Sensitivity of metal nanoparticle surface plasmon resonance to the dielectric environment. *J. Phys. Chem. B* **2005**, *109* (46), 21556−21565.
(43) Manrique-Bedoya, S.; Abdul-Moqueet, M.; Lopez, P.; Gray, T.; Disiena, M.; Locker, A.; Kwee, S.; Tang, L.; Hood, R. L.; Feng, Y.; et al. Multiphysics Modeling of Plasmonic Photothermal Heating Effects in Gold Nanoparticles and Nanoparticle Arrays. *J. Phys. Chem. C* **2020**, *124* (31), 17172−17182.
(44) Coppens, Z. J.; Li, W.; Walker, D. G.; Valentine, J. G. Probing and Controlling Photothermal Heat Generation in Plasmonic Nanostructures. *Nano Lett.* **2013**, *13* (3), 1023−1028.
(45) Mondal, S.; Luis Montaño-Priede, J.; Tu Nguyen, V.; Park, S.; Choi, J.; Hoang Minh Doan, V.; Mai Thien Vo, T.; Hung Vo, T.; Large, N.; Kim, C.-S.; et al. Computational analysis of drug free silver triangular nanoprism theranostic probe plasmonic behavior for in-situ tumor imaging and photothermal therapy. *J. Adv. Res.* DOI: 10.1016/j.jare.2022.02.006.

https://doi.org/10.1021/acs.jpcc.2c03881
J. Phys. Chem. C 2022, 126, 13986−13993